

Na-β-Al₂O₃ stabilized Fe₂O₃ oxygen carriers for chemical looping water splitting: correlating structure with redox stability

Received 00th January 20xx,
Accepted 00th January 20xx

Nur Sena Yüzbaşı^a, Andac Armutlulu^a, Thomas Huthwelker^b, Paula M. Abdala^{*,a}, Christoph R. Müller^{*,a}

DOI: 10.1039/x0xx00000x

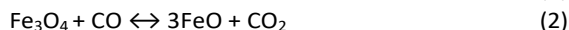
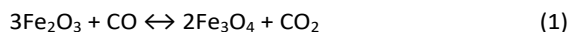
Chemical looping is an emerging technology to produce high purity hydrogen from fossil fuels or biomass with the simultaneous capture of the CO₂ produced at the distributed scale. This process requires the availability of stable Fe₂O₃-based oxygen carriers. Fe₂O₃-Al₂O₃ based oxygen carriers exhibit a decay in the H₂ yield with cycle number due to the formation of FeAl₂O₄ that cannot be re-oxidized. In this study, the addition of sodium (via a sodium salt) in the synthesis of Fe₂O₃-Al₂O₃ oxygen carriers was assessed as a means to counteract the cyclic deactivation of the oxygen carrier. Detailed insight into the oxygen carrier's structure was gained by combined X-ray powder diffraction (XRD), X-ray absorption spectroscopy (XAS) at the Al, Na and Fe K-edges and scanning transmission electron microscopy/energy-dispersive X-ray spectroscopy (STEM/EDX) analyses. The addition of sodium prevented the formation of FeAl₂O₄ and stabilized the oxygen carrier via the formation of a layered structure, Na-β-Al₂O₃ phase. The resulting material, Na-β-Al₂O₃ stabilized Fe₂O₃, showed a very high H₂ yield of ca. 13.3 mmol/g during 15 cycles.

Introduction

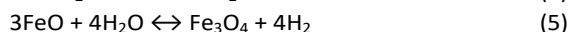
Hydrogen is an emerging energy carrier with potential applications in the transport, industry and power sectors as a fuel that yields water vapour as the only combustion product. If produced sustainably, H₂ has the potential to become a near-zero emission energy carrier, hence reducing energy-related CO₂ emissions.¹⁻³ Currently, the majority of H₂ is produced from natural gas via steam methane reforming (SMR) without carbon dioxide capture, which is an energy intensive process and emits a significant amount of CO₂.^{3, 4} In addition, further energy-intensive purification steps are required to obtain H₂ of sufficiently high purity allowing its use in polymer electrolyte membrane fuel cells (PEMFC).^{5, 6} Hence, for H₂ to become an energy carrier in a sustainable framework, it must be produced in an efficient and sustainable manner, *i.e.* from renewable sources or with CO₂ capture.^{7, 8}

A chemical looping (CL) scheme based on the cyclic redox reactions of iron oxide/iron offers the possibility to produce high purity H₂ with inherent CO₂ capture (Figure 1a).⁷⁻¹⁴ In this process, CO or synthesis gas (a mixture of CO and H₂) is used to reduce Fe₂O₃ to lower oxidation states (ideally to metallic Fe which gives the highest H₂ yield), following reactions 1-3. During Fe₂O₃ reduction, a pure stream of CO₂ is obtained readily through the condensation of water vapour. The oxidation of metallic Fe with steam produces H₂ (water splitting reactions 4 and 5) of high purity.¹⁵ To close the cycle, Fe₃O₄ is oxidized to Fe₂O₃ in air (reaction 6).

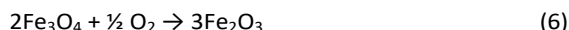
Reduction of iron oxide in CO



Oxidation in steam



Oxidation in air



Owing to its favourable thermodynamics iron oxide is one of the most attractive oxygen carriers for the chemical-looping based production of hydrogen.^{7-11, 13, 15-25} However, pure Fe₂O₃ shows a rapid decay in its H₂ yield with number of redox cycles owing to sintering.¹⁵ Sintering leads to an appreciable decrease in the reduction rate of iron oxide, which results in an incomplete reduction and in turn a low H₂ yield in the subsequent re-oxidation step.^{7, 25, 26} To mitigate deactivation by sintering, strategies based on the addition of a high Tammann temperature stabilizing oxide, *e.g.* Al₂O₃,^{7, 10, 20, 24, 27} SiO₂,^{7, 9} TiO₂,²⁸ CeO₂,¹⁴ MgAl₂O₄^{19, 29} and ZrO₂.^{13, 21, 25} have been proposed. Indeed, these oxides have shown to increase the stability of iron based oxygen carriers over multiple cycles by reducing FeO_x/Fe particle sintering.²¹ Among the investigated oxides, Al₂O₃ is particularly interesting owing to its relatively low cost, high Tammann temperature of ~885 °C and high mechanical resistance.³⁰⁻³² However, Al₂O₃ can react with iron and iron oxide under CL conditions forming the spinel phase FeAl₂O₄ (hercynite) which leads to a decay in the H₂ yield of the material as it cannot be re-oxidized with steam.^{10, 20, 24}

Approaches to prevent the formation of FeAl₂O₄ during redox operation have included the addition of alkali or alkali earth metal oxides to the oxygen carrier, yet the mechanisms behind the mitigation of FeAl₂O₄ formation remains elusive.^{21, 32, 33} In particular, the effect of the addition of sodium on the redox performance of Fe₂O₃-Al₂O₃ based oxygen carriers is controversially discussed and the underlying mechanisms at the atomic scale that would explain the improved macroscopic

^a Laboratory of Energy Science and Engineering, ETH Zurich, Leonhardstrasse 27, 8092, Zurich, Switzerland. E-mail: abdalap@ethz.ch, muelchri@ethz.ch

^b Swiss Light Source, Paul Scherrer Institut, 5232, Villigen PSI, Switzerland.

† Electronic Supplementary Information (ESI) available: [details of any supplementary information available should be included here]. See DOI: 10.1039/x0xx00000x

redox performance of such oxygen carriers are currently not well understood. For instance, a previous study proposed that formulations based on Fe_2O_3 , Al_2O_3 , Na_2O and/or MgO could potentially hinder the formation of FeAl_2O_4 by forming NaAlO_2 or MgAl_2O_4 phases that are thermodynamically more stable²⁹. Indeed, X-ray powder diffraction (XRD) analysis confirmed the presence of NaAlO_2 and MgAl_2O_4 phases in the two studied oxygen carriers with compositions $\text{Na}:\text{Al}:\text{Fe} = 0.25:0.25:0.50$ and $\text{Na}:\text{Mg}:\text{Fe}:\text{Al} = 0.20:0.15:0.28:0.37$ (molar ratios). However, it was found that only MgAl_2O_4 effectively hindered the formation of inactive FeAl_2O_4 while NaAlO_2 only partially prevented its formation. This was explained by the gradual replacement of Al^{3+} by Fe^{3+} in NaAlO_2 ($\text{NaAl}_{1-\gamma}\text{Fe}_\gamma\text{O}_2$) during redox cycling leading to the formation of free Al_2O_3 that subsequently reacts with FeO_x to form FeAl_2O_4 . A further study found that the addition of sodium in concentrations below 5 wt. % stabilizes the reactivity of Fe_2O_3 , yet the structure of the oxygen carriers was not studied in detail.^{18, 34} Typically, X-ray powder diffraction (XRD) has been applied to identify the phases present in the oxygen carrier, however, this analysis fails at describing the local structure of the materials and it is insensitive to amorphous phases and phases in low concentration. Thus, the fine structural features of Na-modified $\text{Fe}_2\text{O}_3\text{-Al}_2\text{O}_3$ oxygen carriers remain elusive.

As discussed above, a difficulty in improving our understanding of the effect of the addition of sodium to $\text{Fe}_2\text{O}_3\text{-Al}_2\text{O}_3$ on its redox behaviour is the lack of knowledge of the atomic-scale structure of these materials. Thus, this work aims at shedding light on the structure-performance relationships of sodium modified $\text{Fe}_2\text{O}_3\text{-Al}_2\text{O}_3$ oxygen carriers for H_2 -production by addressing the following questions: (i) How is the atomic scale structure of $\text{Fe}_2\text{O}_3\text{-Al}_2\text{O}_3$ based oxygen carriers modified by the addition of Na? (ii) What is the Na, Al and Fe environment in the oxygen carrier? and (iii) How does the redox performance relate to the oxygen carriers' structure? To address these questions we performed a detailed structural and redox analysis of sodium modified $\text{Fe}_2\text{O}_3\text{-Al}_2\text{O}_3$ and a sodium free benchmark utilizing XRD and X-ray absorption spectroscopy (XAS) data at the Fe, Al and Na K-edges.

Experimental

Synthesis of the oxygen carriers.

$\text{Fe}_2\text{O}_3\text{:Al}_2\text{O}_3$ and Na-modified $\text{Fe}_2\text{O}_3\text{:Al}_2\text{O}_3$ oxygen carriers were synthesized using a sol-gel method²⁰ with the following compositions: i) $\text{Fe}:\text{Al}$ molar ratio: 0.66:0.34 (75 wt. % Fe_2O_3 , 25 wt. % Al_2O_3), referred to as FeAl; ii) $\text{Na}:\text{Fe}:\text{Al} = 0.02:0.66:0.32$ (76 wt. % Fe_2O_3 , 23 wt. % Al_2O_3 , 1 wt. % Na_2O), referred to as FeAlNa1; and iii) $\text{Na}:\text{Fe}:\text{Al} = 0.11:0.64:0.25$ (76 wt. % Fe_2O_3 , 19% wt. % Al_2O_3 and 5 wt. % Na_2O), referred to as FeAlNa5, (Table S1). In a typical synthesis, aluminum isopropoxide ($\text{Al}(\text{OCH}(\text{CH}_3)_2)_3$, purity ≥ 98 wt. %) was mixed with water and the mixture was hydrolysed for two hours at 75 °C under constant stirring. Nitric acid was used to peptize the slurry. The required amount of the iron and sodium precursors, iron nitrate ($\text{Fe}(\text{NO}_3)_3 \cdot 9\text{H}_2\text{O}$, purity ≥ 98 wt. %) and sodium nitrate (NaNO_3 ,

purity ≥ 99 wt. %) respectively, were mixed with water to obtain a 1 M solution that was added subsequently to the slurry and refluxed for 12 h at 90 °C. The molar ratio of $\text{Al}^{3+}:\text{H}_2\text{O}:\text{H}^+$ was fixed to 0.5:50:0.07. The resulting gel was dried at 100 °C overnight to remove the solvents. A xerogel was obtained after calcination at 900 °C for 2 hours. The calcined materials were crushed and sieved to a particle size range of 300 – 425 μm for further characterization.

Reference materials for structural characterization.

The following reference materials for XAS analysis were synthesized. Na- $\beta\text{-Al}_2\text{O}_3$, with a molar ratio of $\text{Na}:\text{Al} = 1:11$ ($\text{NaAl}_{11}\text{O}_{17}$, $\text{P6}_3/\text{mmc}$ space group³⁹) was synthesized by mixing stoichiometric amounts of $\gamma\text{-Al}_2\text{O}_3$ and Na_2CO_3 followed by calcination at 1350 °C for 6 hours. Na- $\gamma\text{-Al}_2\text{O}_3$ (sodium dispersed at the surface of $\gamma\text{-Al}_2\text{O}_3$) with a molar ratio of $\text{Na}:\text{Al} = 1:15$ was synthesized by wet impregnation of a solution of NaNO_3 (purity > 99 wt. %) onto $\gamma\text{-Al}_2\text{O}_3$. The material was dried at 100 °C in an oven overnight, followed by calcination at 900 °C for 2 h. In addition, commercially available $\alpha\text{-Al}_2\text{O}_3$ (Alfa Aesar, Aluminum oxide, α -phase, 99.9% metal basis) and $\gamma\text{-Al}_2\text{O}_3$ (Alfa Aesar, aluminum oxide, γ -phase, 99.98% metal basis) were utilized as reference materials. The XRD pattern of the references Na- $\beta\text{-Al}_2\text{O}_3$, Na- $\gamma\text{-Al}_2\text{O}_3$, $\alpha\text{-Al}_2\text{O}_3$ and $\gamma\text{-Al}_2\text{O}_3$ are provided in Figure S1. All of the materials were exposed to ambient conditions before characterization. Thus, ambient humidity likely hydrated the surface of all studied oxygen carriers and references, and possibly also the interlayers in the case of Na- $\beta\text{-Al}_2\text{O}_3$.

Characterization of the oxygen carriers.

The crystalline phases of the calcined and cycled oxygen carriers were studied by X-ray diffraction (XRD), using a PANalytical Empyrean X-ray Powder Diffractometer, equipped with a X'Celerator Scientific ultra-fast line detector and Bragg-Brentano HD incident beam optics using Cu K_α radiation (45 kV and 40 mA). A secondary monochromator was employed to suppress unwanted fluorescence originating from iron. Patterns were collected in the range of $2\theta = 5\text{-}90^\circ$, with a step size of $0.016^\circ/\text{s}$ and a total acquisition time of 4 h. Rietveld refinements were performed using FullProf software³⁵.

The local structure of the materials was characterized by XAS at the Fe, Na and Al K-edges. The Na K-edge and Al K-edge XAS measurements were carried out at the Phoenix II, elliptical undulator beamline at the Swiss Light Source (SLS) at the Paul Scherrer Institute (PSI), Switzerland. In a typical experiment a small quantity of material was pressed onto an indium foil and fixed to a copper plate³⁶. XAS measurements were performed in fluorescence mode. The X-ray fluorescence signal was detected using a 1-element Si-drift diode detector SDD (Ketec, Germany). Total electron yield was also collected in the case of Al K-edge measurements. In samples with a high content of absorbing atoms, *i.e.* non-diluted and not thin enough samples, the fluorescence detected XAS signal was corrected due to self-absorption. The current of the incoming beam (I_0) was measured using the total electron yield signal from a 0.5 μm thin polyester foil that was coated with a 50 nm thick layer of nickel. The beam passed through this foil approximately 1 m upstream of the sample in a vacuum chamber held at $\sim 10^{-6}$ mbar. Self-

absorption correction in the Al K-edge spectra was applied. The Fe K-edge XAS spectra were collected at the BM31 beamline at the ESRF, Grenoble, France. The samples were ground, mixed with cellulose to optimize for X-ray absorption and pelletized. The data were collected in transmission mode using a Si (111) double crystal monochromator. Post-processing, self-absorption correction and analysis of the XAS data were performed using the Demeter 0.9.20 software package.³⁷ High-resolution field emission scanning electron microscopy (Zeiss ULTRA 55 plus) was employed to visualize the surface morphology of the oxygen carriers before and after cyclic redox tests. Furthermore, elemental mapping of the synthesized materials was achieved via a Leo Gemini 1530 SEM equipped with an energy dispersive X-ray spectrometer (EDX). A FEI Talos F200X operated at 200 kV was used in both transmission electron microscopy (TEM) and scanning TEM (STEM) modes, with a probe size of approximately 0.8 nm. The instrument is equipped with SuperX EDX comprising four SDD detectors. The STEM/EDX analyses were complemented with atomic number sensitive, high angle annular dark field (HAADF) STEM. The surface area as well as the pore size distribution of the calcined oxygen carriers were determined using a Quantochrome NOVA 4000e N₂ adsorption analyser. The samples were degassed at 300 °C for two hours prior to the acquisition of the N₂ isotherms. The Brunauer-Emmett-Teller (BET)³⁸ and Barrett-Joyner-Halenda (BJH)³⁹ models were used to calculate, respectively, the surface area and the pore size distribution of the materials.

Redox performance.

Cyclic redox experiments were performed in a packed bed reactor, as described in detail in a previous study²³. A typical redox cycle consists of the following steps: (i) reduction in CO (10 vol. % CO in N₂) for 15 minutes (1.5 L/min), (ii) purging with N₂ (1.5 L/min) for 1 minute, (iii) oxidation of the reduced oxygen carrier with steam (23 vol. % H₂O in N₂) for 7 minutes (1.94 L/min), (iv) purging with N₂ (1.5 L/min) for 1 minute, and (v) oxidation with 5 vol. % O₂ in N₂ (2 L/min) for 5 minutes.

Results and Discussion

First, we discuss the cyclic redox behaviour of the synthesized oxygen carriers to determine the effect of the addition of sodium on the redox performance of the materials. Subsequently, we probe in detail the structure of the oxygen carriers in the calcined stated and after exposure to 15 redox cycles to establish structure – performance correlations.

Cyclic redox performance.

The cyclic redox performance of the oxygen carriers was assessed over 15 redox cycles in a packed bed reactor at 800 °C. In each cycle, the oxygen carriers were reduced in CO (10 vol. % CO in N₂) and oxidized first in H₂O (23 vol. % H₂O in N₂) and in a second step in O₂ (5 vol. % O₂ in N₂). For each cycle, the H₂ yield during steam oxidation was calculated by integrating the molar flowrate of H₂ produced (obtained from off-gas concentration profiles) with respect to time by using equation 7:²¹

$$N_{H_2} = \dot{N}_{N_2} \times \int \frac{y_{H_2}}{1-y_{H_2}} dt \quad (7)$$

where N_{H_2} is the number of moles of H₂ produced, \dot{N}_{N_2} is the molar flow rate of N₂, and y_{H_2} is mole fraction of H₂ in the gas leaving the packed bed.

The H₂ yield expressed as mmol H₂/g of oxygen carrier as a function of cycle number is given in Figure 1. The H₂ yield of FeAl decreased rapidly over 15 cycles from 12.7 mmol H₂/g oxygen carrier in the first cycle, to 11.1 mmol H₂/g oxygen carrier in the fifth cycle and to 6 mmol H₂/g oxygen carrier in the fifteenth cycle. The addition of sodium enhanced the redox stability of FeAlNa1 and increased the H₂ yield compared to FeAl; however, from the eighth redox cycle onwards also for this material the H₂ yield started to decrease. A more pronounced stabilization effect was observed in FeAlNa5. The H₂ yield of FeAlNa5 was stable over 15 redox cycles and was close to the theoretically

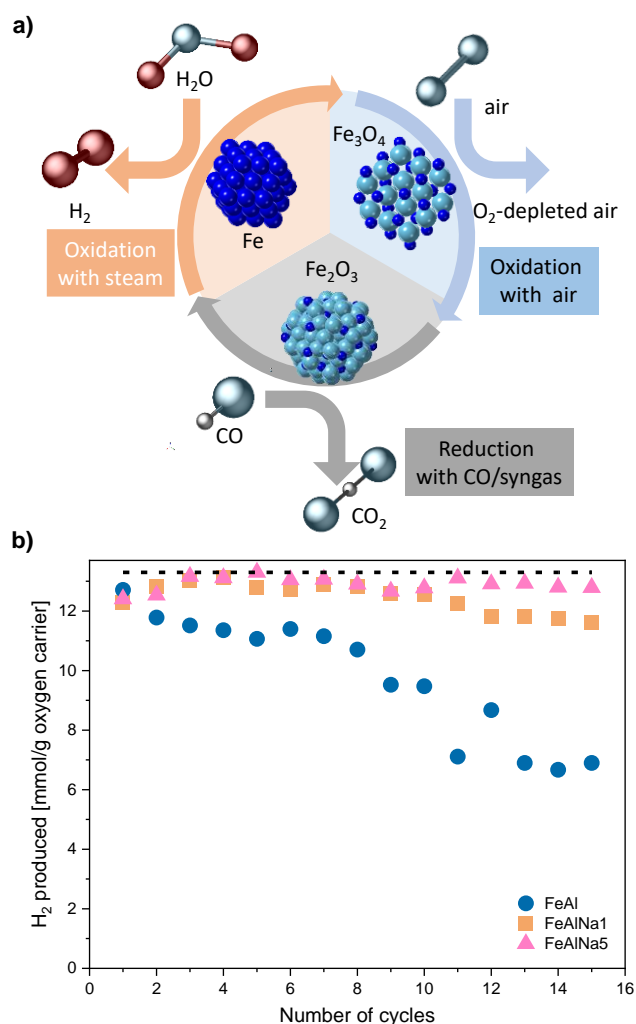


Figure 1. (a) Schematic of the Fe₂O₃-Fe based chemical looping process for the production of H₂ using a synthesis gas (H₂ and CO) as the fuel. (b) H₂ yield as a function of cycle number for FeAl, FeAlNa1 and FeAlNa5. The redox experiments were performed at 800 °C in a packed-bed reactor using 10 vol. % CO in N₂ for reduction and 23 vol. % H₂O in N₂ followed by 5 vol. % O₂ in N₂ for re-oxidation. The dashed horizontal line represents the theoretically expected H₂ yield (13.3 mmol/g) for an oxygen carrier that contains 80 wt. % Fe₂O₃.

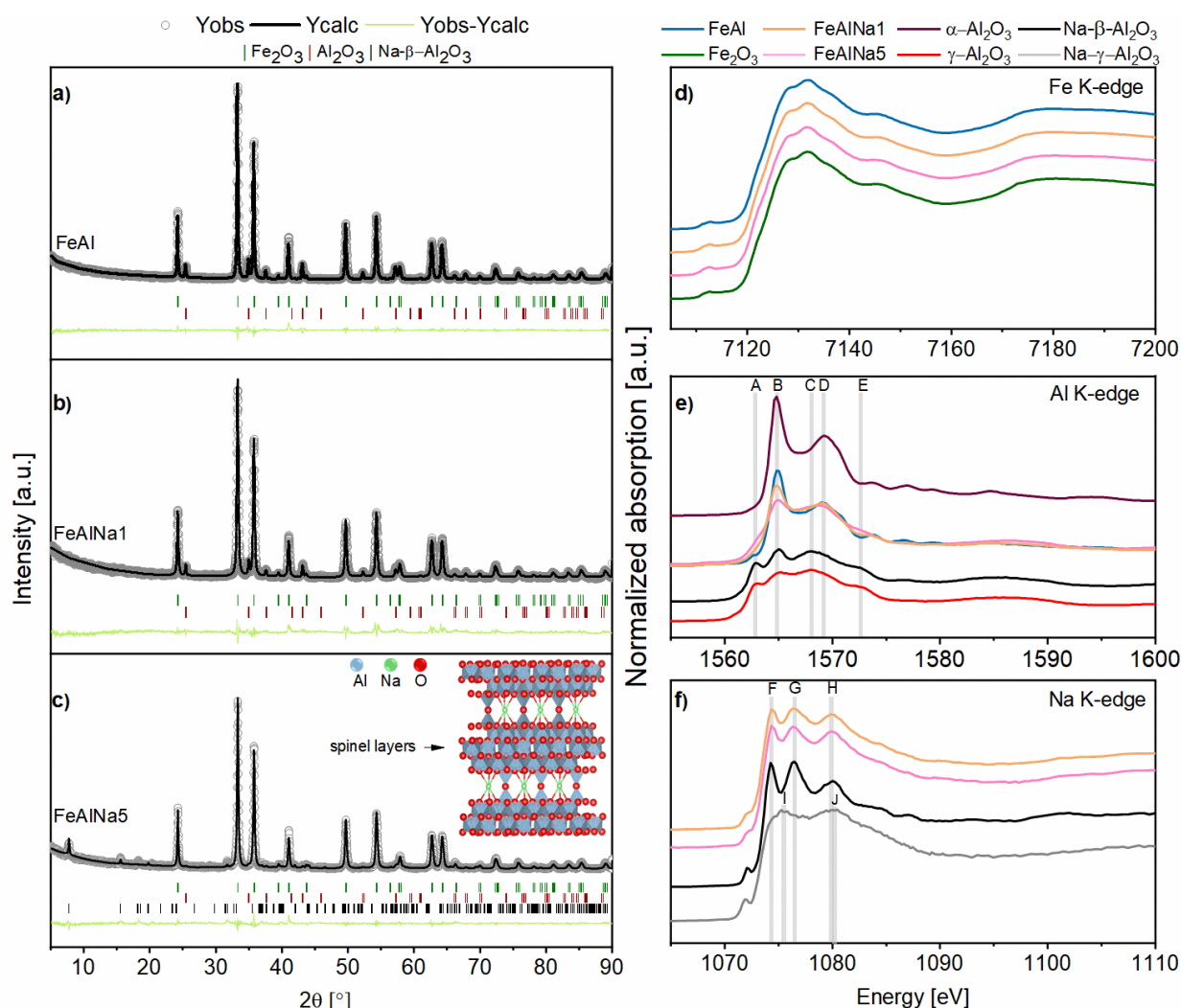


Figure 2: (a-c) XRD patterns of the calcined oxygen carriers and the corresponding Rietveld refinements. The inset in (c) sketches the crystal structure of Na-β-Al₂O₃ containing layers of γ-alumina that are connected by bridging oxygen and sodium ions. XANES spectra at the (d) Fe K-edge, (e) Al K-edge, (f) Na K-edge of the calcined oxygen carriers and reference materials.

expected value of 13.3 mmol/g oxygen carrier. These results show that the introduction of sodium has a large impact on the cyclic behaviour of Al₂O₃ stabilized, Fe₂O₃-based oxygen carriers. To obtain insight into the origin of the improved redox stability of FeAlNa1 and FeAlNa5 compared to FeAl, the morphological and structural characteristics of the calcined and cycled materials (15 cycles) were probed by XRD, XAS and STEM/EDX.

Structure of the calcined and cycled oxygen carriers by XRD and XAS

Calcined oxygen carriers

XRD analysis confirms that the main crystalline component in all of the calcined materials is hematite α-Fe₂O₃ (Figure 2a and Table S2). Additionally, α-Al₂O₃ (corundum) is observed in FeAl and FeAlNa1. In the case of FeAlNa5, there are also reflections due to α-Al₂O₃ observable; however, with a very weak intensity. In addition, FeAlNa5 contains a third phase, *i.e.* Na-β-Al₂O₃ (P6₃/mmc space group, Figure 2b) ⁴⁰. Rietveld refinement allowed us to quantify the fraction of the crystalline phases in

the oxygen carriers and to determine the cell parameters of these phases. The unit cell parameters of α-Fe₂O₃ and α-Al₂O₃ are reported in Table S2 and did not change (within the experimental error) upon the addition of sodium (Figure 2 and Table S2). The fact that the cell parameters are invariant with the addition of Na suggests that sodium is not incorporated into the crystal structures of α-Fe₂O₃ or α-Al₂O₃. The determined cell parameters of Na-β-Al₂O₃ (*a* = *b* = 5.6385 Å and *c* = 22.816 Å) is in a good agreement with previous studies ⁴⁰⁻⁴². The weight fractions of α-Al₂O₃ in the calcined materials were determined as 27, 23 and 3 wt. % for FeAl and FeAlNa1 and FeAlNa5 respectively, *i.e.* the fraction of α-Al₂O₃ decreased with increasing Na content. For FeAl and FeAlNa1, α-Fe₂O₃ balanced the phase composition of the oxygen carriers, amounting to, respectively, 73 and 77 wt. % α-Fe₂O₃. For FeAlNa5, the refined phase composition was 82 wt. % α-Fe₂O₃, 15 wt. % Na-β-Al₂O₃ and 3 wt. % α-Al₂O₃. The presence of Na-β-Al₂O₃ in FeAlNa1 was not evidenced by XRD, yet this might be due to limitations of XRD in determining phases of low concentrations and/or poor

crystallinity. To obtain further insight into the effect of the addition on sodium on the phase composition and structure of the oxygen carriers, we turned to an element specific technique X-ray technique, *i.e.* XAS at the Fe, Na and Al K-edges.

First, we analysed the local environment around iron. Fe K-edge XANES (X-ray absorption near edge structure) spectra of the calcined oxygen carriers are provided in Figure 2d. The spectra of all of the oxygen carriers contain the same features as the α -Fe₂O₃ reference. The EXAFS (extended X-ray absorption fine structure) functions and the corresponding Fourier transforms (FT) are given in Figure S2 and further confirm that the local environment around Fe corresponds to the local Fe environment in α -Fe₂O₃ in all three calcined materials. Hence, the XAS data confirm that the local environment of Fe is not affected by the presence of sodium. Importantly, it also shows that there is no formation of a solid solution or mixed oxide between Fe₂O₃ and Al₂O₃ upon calcination at 900 °C.

Figure 2e displays the Al K-edge XANES spectra of the oxygen carriers and reference materials. To interpret these XANES data we will first discuss the XANES data of the reference materials α -Al₂O₃, γ -Al₂O₃ and Na- β -Al₂O₃. The crystal structure of α -Al₂O₃ is described by a hexagonal unit cell with Al in an octahedral coordination. The corresponding XANES spectrum (Figure 2e) exhibits a doublet peak in the white-line region, with a sharp intense peak at 1565 eV (labelled as B), and a broader feature at 1568 eV (labelled as D), typical for Al in an octahedral coordination and in agreement with previously data^{43, 44}. The reference γ -Al₂O₃ has a defect spinel type structure, in which Al atoms occupy both octahedral and tetrahedral sites⁴⁵. In the XANES spectrum of γ -Al₂O₃, features A, B, C and E are observed at 1563, 1565, 1568 and 1573 eV, respectively. In γ -Al₂O₃ feature B is considerably less intense than in α -Al₂O₃ and feature C has been attributed to tetrahedrally coordinated Al⁴⁶. Na- β -Al₂O₃ is a layered structure containing γ -Al₂O₃ layers that are linked by sodium and oxygen atoms (inset in Figure 2c)^{48, 49}. The fact that the Al K-edge XANES spectrum of Na- β -Al₂O₃ exhibits similar features as γ -Al₂O₃ confirms the presence of γ -Al₂O₃ layers in Na- β -Al₂O₃.⁵⁰

Next, we investigate the Al environment in the three oxygen carriers. The Al K-edge XANES spectrum of FeAl shows features B and D, indicating that Al³⁺ is in an octahedral coordination similar to α -Al₂O₃,⁴³⁰ in line with XRD. With increasing sodium content, the intensity of feature B decreases, which implies that the fraction of α -Al₂O₃ in the material decreases with increasing sodium content. In agreement with our previous XRD analysis is the fact that the Al K-edge XANES spectrum of FeAlNa1 is dominated by features due to α -Al₂O₃. On the other hand, in FeAlNa5 features A, C and E are prominent which is indicative of the presence of spinel-type γ -Al₂O₃ or Na- β -Al₂O₃ (according to XRD). Features A, C and E are also present in FeAlNa1, but with a considerably lower intensity. Hence, our XANES results indicate that FeAlNa1 and FeAlNa5 contain a mixture of α -Al₂O₃ and a spinel-type Al₂O₃ phase. While α -Al₂O₃ is the main Al-based phase in FeAlNa1, Na- β -Al₂O₃ (or γ -Al₂O₃) is the main Al-containing phase in FeAlNa5. Na- β -Al₂O₃ and γ -Al₂O₃ share the same Al K-edge features, yet combining the information of XRD

and Na-Kedge XAS (*vide infra*), we assign the observed features to Na- β -Al₂O₃ rather than to γ -Al₂O₃.

Lastly, we assess the Na environment in the oxygen carriers and reference materials. The Na K-edge XANES spectrum of Na- β -Al₂O₃ exhibits three main peaks labelled as F, G and H, located at 1074, 1076 and 1080 eV, respectively (Figure 2f). To the best of our knowledge, this is the first experimentally collected Na K-edge spectrum of Na- β -Al₂O₃. The spectrum of Na- γ -Al₂O₃ (*i.e.* the reference material prepared by wet impregnation of a solution of NaNO₃ onto γ -Al₂O₃) shows features different to Na- β -Al₂O₃ and are labelled I (1075 eV) and J (1080 eV) (Figure S3). These Na K-edge XANES features of Na- γ -Al₂O₃ are assigned to Na ions dispersed on the surface of γ -Al₂O₃ (in a solvated state).⁵¹ Thus, using Na K-edge XANES we can distinguish between two different Na environments: (i) a Na- β -Al₂O₃ like environment, *i.e.* Na that is located between layers of γ -Al₂O₃ layers (ordered) and (ii) a Na- γ -Al₂O₃ like environment in which Na is located on the surface of γ -Al₂O₃ (surface Na⁺). The Na K-edge XANES spectra of FeAlNa1 and FeAlNa5 exhibit features F, G and H at, respectively 1074.4 eV (A), 1076.4 eV (B) and 1080.2 eV (C), suggesting a similar Na local environment in these two calcined oxygen carriers as in Na- β -Al₂O₃ (Figure 2f). The presence of Na- β -Al₂O₃ in FeAlNa5 aligns with XRD results. The absence of diffraction peaks due to Na- β -Al₂O₃ in FeAlNa1 is possibly linked to its small quantity in FeAlNa1. However, we noticed that the features F, G and H in the Na K-edge XANES spectra of FeAlNa1 and FeAlNa5 are less intense compared to the reference Na- β -Al₂O₃. This is possibly due to the presence of two different Na environments in the calcined oxygen carriers. This observation led us to propose that the Na K-edge XANES spectra of the oxygen carriers can be fitted by a linear combination of Na in an environment of Na- β -Al₂O₃ and surface Na⁺ in the form of Na- γ -Al₂O₃. Indeed, linear combination fitting yielded Na to be ca. 60 % in a Na- β -Al₂O₃ environment and 40 % in a Na- γ -Al₂O₃ type environment in both FeAlNa1 and FeAlNa5 (Figure S4).

Cycled oxygen carriers

To probe in depth the effect of sodium-containing phases on the redox stability of the Fe₂O₃-Al₂O₃ system the structures of the oxygen carriers that have undergone 15 redox cycles were also characterized XRD and XAS. The cycled oxygen carriers were analysed in their reduced state as it has been argued that the presence of sodium hinders the formation of inactive hercynite during reduction^{10, 20, 24}.

The cycled materials (labelled with _cyc) exhibit dominant Bragg reflections due to fcc-Fe (Figure 3a). However, the presence of magnetite (Fe₃O₄), wuestite-FeO (only in FeAl) and hercynite (spinel FeAl₂O₄) in FeAl_{cyc} and FeAlNa1_{cyc} points to an incomplete reduction. Importantly, the XRD pattern of FeAlNa5_{cyc} does not show peaks due to FeAl₂O₄, but peaks due to Na- β -Al₂O₃ (Figure 3a), indicating that Na- β -Al₂O₃ is stable under redox conditions. The XANES spectra and FT-EXAFS functions of the three cycled oxygen carriers are shown in Figure 3 and Figure S5, respectively. From the increase in the intensity of the white line it is clear that the degree of reduction followed the order FeAl_{cyc} < FeAlNa1_{cyc} < FeAlNa5_{cyc}. The Fe K-edge XANES spectra (Figure 3b) of the oxygen carriers were fitted by a linear combination of an Fe foil, FeO and FeAl₂O₄ and

yielded 48, 79 and 94 wt. % metallic Fe⁰ in, respectively, FeAl_{cyc}, FeAlNa1_{cyc} and FeAlNa5_{cyc}. These results confirm that in FeAlNa5 the formation of FeAl₂O₄ during reduction is hindered and iron oxide can be reduced almost completely over 15 redox cycles. To some extent, there is also a stabilization effect in FeAlNa1, yet the formation of FeAl₂O₄ could not be avoided fully. This is in line with the drop in the hydrogen yield of FeAlNa1 with cycle number.

Turning to the analysis of the Al K-edge XANES data of the cycled oxygen carriers, we did not observe any signatures due to α -Al₂O₃ in any of the cycled oxygen carriers, instead features characteristic of spinel type phases are present. The Al K-edge XANES spectrum of FeAlNa5_{cyc} (Figure 3c) shows the same characteristic features as the Na- β -Al₂O₃ reference (Figure 2e). This indicates that during redox cycling the small fraction of α -Al₂O₃ that was initially present in calcined FeAlNa5 transforms fully to Na- β -Al₂O₃. Comparing the spectrum of FeAlNa5_{cyc} with the spectra of FeAl_{cyc} and FeAlNa1_{cyc} revealed a more intense feature at ca. 1569.6 eV for FeAl_{cyc} and FeAlNa1_{cyc} (marked with an arrow in Figure 3c). This feature can be attributed to the substitution of Al sites by Fe in a spinel structure in analogy to the spinel MgAl₂O₄⁴⁶ which is isostructural to FeAl₂O₄. Hence, consolidating with our XRD and Fe K-edge XAS results, the feature at 1569.6 eV in the Al K-edge XANES spectra of FeAl_{cyc} and FeAlNa1_{cyc} is attributed to the formation of FeAl₂O₄.

The Na K-edge XANES spectra of the cycled materials are shown in Figure 3d. We observe that in FeAlNa5_{cyc} the local environment of Na in the form of Na- β -Al₂O₃ is preserved during redox cycling. This is evidenced by the presence of the three features F, G and H in FeAlNa5_{cyc}. Linear combination fitting of the spectrum of FeAlNa5_{cyc} yields 71% of Na in a Na- β -Al₂O₃ framework and 29% of Na in the form of surface Na (Na- γ -Al₂O₃ type). Hence, the fraction of Na in a Na- β -Al₂O₃-type environment in FeAlNa5 increases with redox cycling, in line with Al K-edge XANES analysis. On the other hand, the Na K-edge XANES spectrum of FeAlNa1_{cyc} exhibits, compared to FeAlNa5, a different change in the Na environment with redox cycling. The three sharp features (labelled F, G and H) in calcined FeAlNa1 are not detected in FeAlNa1_{cyc} (Figure S6). Instead a broader doublet (features I and J) at 1075 and 1080.5 eV appears after redox cycling, indicative that FeAlNa1_{cyc} closely resembles the spectrum of the Na- γ -Al₂O₃ reference. This change in the local environment of Na upon redox cycling, indicates that in FeAlNa1 Na is initially present in a Na- β -Al₂O₃ like environment (in the layered structure), but migrates and disperses on the material's surface during redox cycling.

Morphology and elemental mapping of the calcined and cycled carriers.

The morphology of the freshly calcined oxygen carriers, as probed by electron microscopy is affected only marginally by the addition of sodium (Figure S7). The calcined oxygen carriers FeAl, FeAlNa1 and FeAlNa5 were composed of particles with an average grain size of $\sim 100 \pm 20$ nm (based on the analysis of 50 particles). The weight composition of the materials as determined by SEM/EDX (Table S1) are in good agreement with the nominal compositions of the oxygen carriers. The elemental

mapping of the oxygen carriers revealed that the sol-gel synthesis led to a high dispersion of Fe, Na and Al, indicating that the different phases were highly dispersed in the materials (Figure S8). The calcined oxygen carriers FeAl, FeAlNa1 and FeAlNa5 have similar BET surface areas and BJH pore volumes (Table S1).

HAADF-STEM images and the corresponding EDX maps of Fe, Al and Na are given in Figure 4. In the calcined materials FeAl, FeAlNa1, and FeAlNa5, discrete Fe₂O₃- and Al₂O₃-rich particles are formed, and Na is distributed evenly in FeAlNa1. In FeAlNa5, the EDX signals of Al and Na overlap, which is in line with the outcome of the XRD and XAS analysis (Figure 2a) pointing to the formation of a Na- β -Al₂O₃ phase. Similarly, the EDX maps of FeAl_{cyc} and FeAlNa1_{cyc} show overlapping signals of Fe and Al, which are in agreement with the formation of the spinel FeAl₂O₄ as determined by XRD and XAS. No such overlap is observed in FeAlNa5_{cyc}, which features discrete Al- and Fe-rich particles. Furthermore, the overlapping signals of Na and Al in FeAlNa5_{cyc} provide further evidence for the formation of Na- β -Al₂O₃ as determined by the XRD and XAS analyses.

Structure-performance relationships

Combining the results of the cyclic redox tests, with our XRD, XAS and HAADF-STEM-EDX analyses we can propose the following structure – performance correlations. The reaction of α -Al₂O₃ with Fe/FeO_x during redox cycling leads to the formation of (inactive) FeAl₂O₄ that in turn correlates with a rapid decay in the H₂ yield in FeAl. The high redox stability of FeAlNa5 correlates with the formation of Na- β -Al₂O₃ and the absence of α -Al₂O₃ in this oxygen carrier. The formation of Na- β -Al₂O₃ in FeAlNa5 hinders effectively the formation of FeAl₂O₄ during repeated redox cycles, leading in turn to a material with a stable hydrogen yield. The Na- β -Al₂O₃ phase is stable and reductive and oxidative environments and is highly dispersed within the Fe/FeO_x matrix. The oxygen carrier with a lower Na content, *i.e.* FeAlNa1, shows a dominating presence of α -Al₂O₃ and a small fraction of Na- β -Al₂O₃ initially freshly calcined state. Such a phase composition can only partially stabilize the oxygen carrier. Indeed, in FeAlNa1, Na is initially present in two environments *i.e.* as Na- β -Al₂O₃ and dispersed as surface Na. During the redox cycling of FeAlNa1, all of the α -Al₂O₃ reacts with FeO_x forming FeAl₂O₄, while sodium is found in a non-crystalline form (dispersed at the surface of the particle). Therefore, our study points to the critical role of the layered Na-

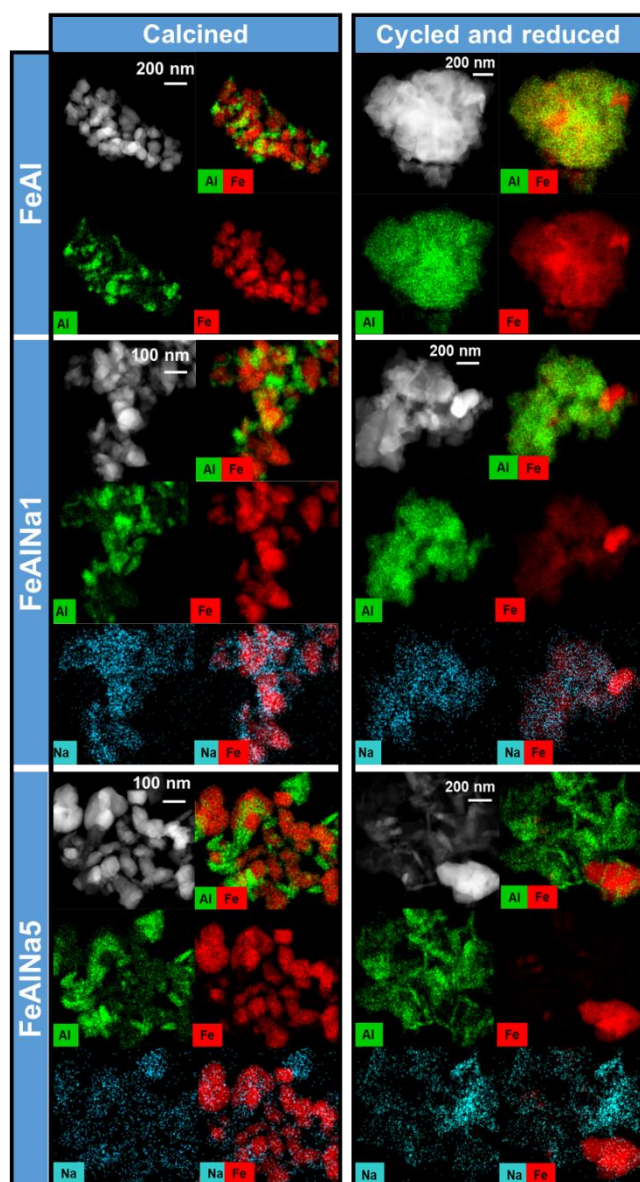


Figure 4. HAADF images and elemental maps (STEM-EDX) of the calcined oxygen carriers and after cycling experiments (15 cycles, reduction step).

β - Al_2O_3 phase in stabilizing the hydrogen yield of Al_2O_3 -stabilized, Fe_2O_3 based oxygen carriers.

Conclusions

In this work, we probe the effect of the addition of sodium to Fe_2O_3 - Al_2O_3 -based oxygen carriers, on their redox stability, phase composition and phase dynamics over redox cycles. Application of XRD, XAS at the Al, Na and Fe K-edges and STEM/EDX to the freshly calcined and cycled materials allowed us to draw the following conclusions:

- i. α - Al_2O_3 reacts with Fe/FeO_x during redox cycling leading to the formation of FeAl_2O_4 ; the formation of which correlates directly with the rapid decrease in the H_2 yield of an oxygen carrier.

- ii. Depending on the loading of sodium in the oxygen carrier, sodium can be found in a crystalline $\text{Na-}\beta$ - Al_2O_3 phase or at the surfaces of the particles.
- iii. Na in the environment of the layered structure $\text{Na-}\beta$ - Al_2O_3 effectively stabilizes the redox performance of an oxygen carrier, while surface sodium cannot prevent fully material deactivation.

This work, demonstrates how probing of the local and average structure, such as multi edge XAS analysis in combination with XRD and electron microscopy allows for the formulation of structure – performance correlations. In addition, this work showcases the application of XAS in the tender X-ray region (Na and Al K-edges) that have not been investigated extensively particularly in the field of chemical looping and can therefore be of interest to the broader functional materials community.

Conflicts of interest

There are no conflicts to declare.

Acknowledgements

The authors would like to acknowledge the Swiss National Science Foundation (406640_136707) and the Swiss Office of Energy (BFE, SI/500652) for financial support. This project has received partial funding from the European Union's Horizon 2020 research and innovation program (grant agreement No 800419). This publication was created as part of NCCR Catalysis, a National Centre of Competence in Research funded by the Swiss National Science Foundation. We also thank to Scientific Centre for Optical and Electron Microscopy (ScopeM) for providing training and access to scanning electron microscopes. The authors are grateful to the Swiss Light Source (SLS) at the Paul Scherrer Institute (Villigen, Switzerland), for providing beamtime at the PHOENIX beamline, and to the European Synchrotron Facility (ESRF) and the Swiss-Norwegian beamline (SNBL at ESRF) for providing beamtime for XAS measurements.

Notes and references

1. BP, Energy Outlook 2017 Edition, 2017.
2. IEA, Technology Roadmap: Hydrogen and Fuel Cells, 2015.
3. J. A. Turner, *Science*, 2004, **305**, 972-974.
4. M. Zerta, P. R. Schmidt, C. Stiller and H. Landinger, *International journal of hydrogen energy*, 2008, **33**, 3021-3025.
5. T. V. Choudhary and D. Goodman, *Catalysis Today*, 2002, **77**, 65-78.
6. G. Postole and A. Auroux, *international journal of hydrogen energy*, 2011, **36**, 6817-6825.
7. C. Bohn, J. Cleeton, C. Müller, S. Chuang, S. Scott and J. Dennis, *Energy & Fuels*, 2010, **24**, 4025-4033.
8. A. Thursfield, A. Murugan, R. Franca and I. S. Metcalfe, *Energ Environ Sci*, 2012, **5**, 7421-7459.
9. Q. Zafar, T. Mattisson and B. Gevert, *Industrial & Engineering Chemistry Research*, 2005, **44**, 3485-3496.

10. P. R. Kidambi, J. P. E. Cleeton, S. A. Scott, J. S. Dennis and C. D. Bohn, *Energy & Fuels*, 2012, **26**, 603-617.
11. J. R. Scheffe, M. D. Allendorf, E. N. Coker, B. W. Jacobs, A. H. McDaniel and A. W. Weimer, *Chemistry of Materials*, 2011, **23**, 2030-2038.
12. R. D. Solunke and G. Vesper, *Industrial & Engineering Chemistry Research*, 2010, **49**, 11037-11044.
13. N. S. Yüzbaşı, P. M. Abdala, Q. Imtiaz, S. M. Kim, A. M. Kierzkowska, A. Armutlulu, W. van Beek and C. R. Müller, *Physical Chemistry Chemical Physics*, 2018, **20**, 12736-12745.
14. L.-S. Fan and F. Li, *Industrial & Engineering Chemistry Research*, 2010, **49**, 10200-10211.
15. C. D. Bohn, C. R. Müller, J. P. Cleeton, A. N. Hayhurst, J. F. Davidson, S. A. Scott and J. S. Dennis, *Industrial & Engineering Chemistry Research*, 2008, **47**, 7623-7630.
16. J. P. E. Cleeton, C. D. Bohn, C. R. Müller, J. S. Dennis and S. A. Scott, *International Journal of Hydrogen Energy*, 2009, **34**, 1-12.
17. D. Hosseini, F. Donat, S. M. Kim, L. Bernard, A. M. Kierzkowska and C. R. Müller, *ACS Applied Energy Materials*, 2018.
18. W.-C. Huang, Y.-L. Kuo, P.-C. Su, Y.-H. Tseng, H.-Y. Lee and Y. Ku, *Chemical Engineering Journal*, 2018, **334**, 2079-2087.
19. Q. Imtiaz, N. S. Yüzbaşı, P. M. Abdala, A. M. Kierzkowska, W. van Beek, M. Broda and C. R. Müller, *Journal of Materials Chemistry A*, 2016, **4**, 113-123.
20. A. Kierzkowska, C. Bohn, S. Scott, J. Cleeton, J. Dennis and C. Müller, *Industrial & Engineering Chemistry Research*, 2010, **49**, 5383-5391.
21. W. Liu, J. S. Dennis and S. A. Scott, *Industrial & Engineering Chemistry Research*, 2012, **51**, 16597-16609.
22. C. Müller, C. Bohn, Q. Song, S. Scott and J. Dennis, *Chemical engineering journal*, 2011, **166**, 1052-1060.
23. J.-b. Yang, N.-s. Cai and Z.-s. Li, *Energy & Fuels*, 2008, **22**, 2570-2579.
24. N. S. Yüzbaşı, A. Kierzkowska and C. Müller, *Energy Procedia*, 2017, **114**, 436-445.
25. N. S. Yüzbaşı, A. M. Kierzkowska, Q. Imtiaz, P. M. Abdala, A. Kurllov, J. L. M. Rupp and C. R. Müller, *The Journal of Physical Chemistry C*, 2016, **120**, 18977-18985.
26. Z. Ma, S. Zhang and R. Xiao, *Energy Conversion and Management*, 2019, **188**, 429-437.
27. M. Ishida, K. Takeshita, K. Suzuki and T. Ohba, *Energy & Fuels*, 2005, **19**, 2514-2518.
28. C. Chung, L. Qin, V. Shah and L.-S. Fan, *Energy Environ Sci*, 2017.
29. W. Liu, M. Ismail, M. T. Dunstan, W. Hu, Z. Zhang, P. S. Fennell, S. A. Scott and J. S. Dennis, *RSC Advances*, 2015, **5**, 1759-1771.
30. M. Arjmand, A.-M. Azad, H. Leion, T. Mattisson and A. Lyngfelt, *Industrial & Engineering Chemistry Research*, 2012, **51**, 13924-13934.
31. J. Adanez, A. Abad, F. Garcia-Labiano, P. Gayan and L. F. de Diego, *Progress in Energy and Combustion Science*, 2012, **38**, 215-282.
32. Q. Imtiaz, P. M. Abdala, A. M. Kierzkowska, W. Van Beek, S. Schweiger, J. L. Rupp and C. R. Müller, *Physical Chemistry Chemical Physics*, 2016, **18**, 12278-12288.
33. Q. Song, W. Liu, C. D. Bohn, R. N. Harper, E. Sivaniyah, S. A. Scott and J. S. Dennis, *Energy Environ Sci*, 2013, **6**, 288-298.
34. L. Liu and M. R. Zachariah, *Energy & Fuels*, 2013, **27**, 4977-4983.
35. J. Rodriguez-Carvajal, *Physica B*, 1993, **192**, 55.
36. M. Galib, M. Baer, L. Skinner, C. Mundy, T. Huthwelker, G. Schenter, C. Benmore, N. Govind and J. L. Fulton, *The Journal of Chemical Physics*, 2017, **146**, 084504.
37. B. Ravel and M. Newville, *J Synchrotron Radiat*, 2005, **12**, 537-541.
38. S. Brunauer, P. H. Emmett and E. Teller, *J Am Chem Soc*, 1938, **60**, 309-319.
39. E. P. Barrett, L. G. Joyner and P. P. Halenda, *J Am Chem Soc*, 1951, **73**, 373-380.
40. N. Zhu, F. Guo, S. Yan, L. Chen and A. Li, *Acta Chimica Sinica*, 1992, **50**, 527-532.
41. W. A. England, A. J. Jacobson and B. C. Tofield, *Solid State Ionics*, 1982, **6**, 21-27.
42. C. Peters, M. Bettman, J. t. Moore and M. Glick, *Acta Crystallographica Section B: Structural Crystallography and Crystal Chemistry*, 1971, **27**, 1826-1834.
43. A. Omegna, R. Prins and J. A. van Bokhoven, *The Journal of Physical Chemistry B*, 2005, **109**, 9280-9283.
44. D. R. Neuville, L. Cormier, A.-M. Flank, V. Briois and D. Massiot, *Chemical Geology*, 2004, **213**, 153-163.
45. R. Prins, *Journal of Catalysis*, 2020, **392**, 336-346.
46. D. R. Neuville, D. De Ligny, L. Cormier, G. S. Henderson, J. Roux, A.-M. Flank and P. Lagarde, *Geochimica et Cosmochimica Acta*, 2009, **73**, 3410-3422.
47. Y. Kato, K.-i. Shimizu, N. Matsushita, T. Yoshida, H. Yoshida, A. Satsuma and T. Hattori, *Physical Chemistry Chemical Physics*, 2001, **3**, 1925-1929.
48. N. Iyi, S. Takekawa and S. Kimura, *Journal of Solid State Chemistry*, 1989, **83**, 8-19.
49. Y. Yung-Fang Yu and J. T. Kummer, *Journal of Inorganic and Nuclear Chemistry*, 1967, **29**, 2453-2475.
50. A. Marcelli, A. Mottana and G. Cibin, *Journal of applied crystallography*, 2000, **33**, 234-242.
51. M. Digne, P. Raybaud, P. Sautet, D. Guillaume and H. Toulhoat, *Physical Chemistry Chemical Physics*, 2007, **9**, 2577-2582.

Supporting information

Table S1: Weight-based composition, surface areas, pore volumes and particle diameters of the materials calcined at 900 °C.

		FeAl	FeAlNa1	FeAlNa5
Nominal weight compositions	Fe₂O₃ (wt. %)	75	76	76
	Al₂O₃ (wt. %)	25	23	19
	Na₂O (wt. %)	-	1	5
	Al₂O₃:Fe₂O₃ ratio	0.33	0.30	0.33
Weight-based compositions calculated from EDX	Fe₂O₃ (wt. %)	77	76.4	73.8
	Al₂O₃ (wt. %)	23	22.5	21.9
	Na₂O (wt. %)		1.1	4.3
	Al₂O₃:Fe₂O₃ ratio	0.30	0.30	0.33
Molar ratios calculated from EDX	Fe	0.96	0.95	0.94
	Al	0.44	0.42	0.42
	Na	-	0.03	0.14
Surface Area [m²/g]		9	17	11
Pore Volume [cm³/g]		0.1	0.19	0.13
Average particle size [nm]		112 ± 35	107 ± 25	100 ± 27

Table S2: Phase composition and cell parameters determined by Rietveld refinement of the XRD data of the calcined oxygen carriers.^a

		a [Å]	b [Å]	c [Å]	Cell volume [Å ³]	Phase content [wt %]	Rp	Rwp	Rexp
FeAl	Fe₂O₃	5.0169(1)	5.0169(1)	13.6849(5)	298.29 (1)	73(1)	6.35	9.07	3.78
	Al₂O₃	4.7851(3)	4.7851(3)	13.054(1)	258.86(3)	27(1)			
FeAlNa1	Fe₂O₃	5.0173(1)	5.0173(1)	13.6898(5)	298.46(2)	77(1)	5.37	7.19	3.79
	Al₂O₃	4.7829(2)	4.7829(2)	13.053(1)	258.59(3)	23(1)			
FeAlNa5	Fe₂O₃	5.0181(1)	5.0181(1)	13.6867(1)	298.48(1)	82(1)	7.07	9.55	3.79
	Al₂O₃	4.782 (1)	4.782(1)	13.047(6)	258.4(1)	3(1)			
	NaAl₁₁O₁₇	5.6385(8)	5.6385(8)	22.816(6)	628.2(2)	15(1)			

Fe₂O₃ phase: *R-3c* space group, with atomic positions as reported in ⁵², Al₂O₃ phase: *R-3c* space group, with atomic positions as reported in ⁵³ and Na-β-Al₂O₃: *P6₃/mmc* space group with atomic positions as reported in ⁴⁰

1. P. Schouwink, L. Dubrovinsky, K. Glazyrin, M. Merlini, M. Hanfland, T. Pippinger and R. Miletich, *American Mineralogist*, 2011, **96**, 1781-1786.
2. S. Kondo, K. Tateishi and N. Ishizawa, *Japanese Journal of Applied Physics*, 2008, **47**, 616.
3. N. Zhu, F. Guo, S. Yan, L. Chen and A. Li, *Acta Chimica Sinica*, 1992, **50**, 527-532.

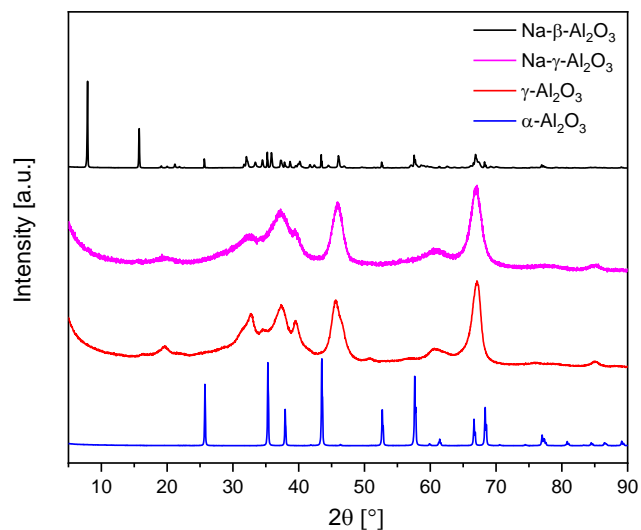


Figure S1: XRD patterns of the reference materials: γ -Al₂O₃, α -Al₂O₃, Na- γ -Al₂O₃ and Na- β -Al₂O₃.

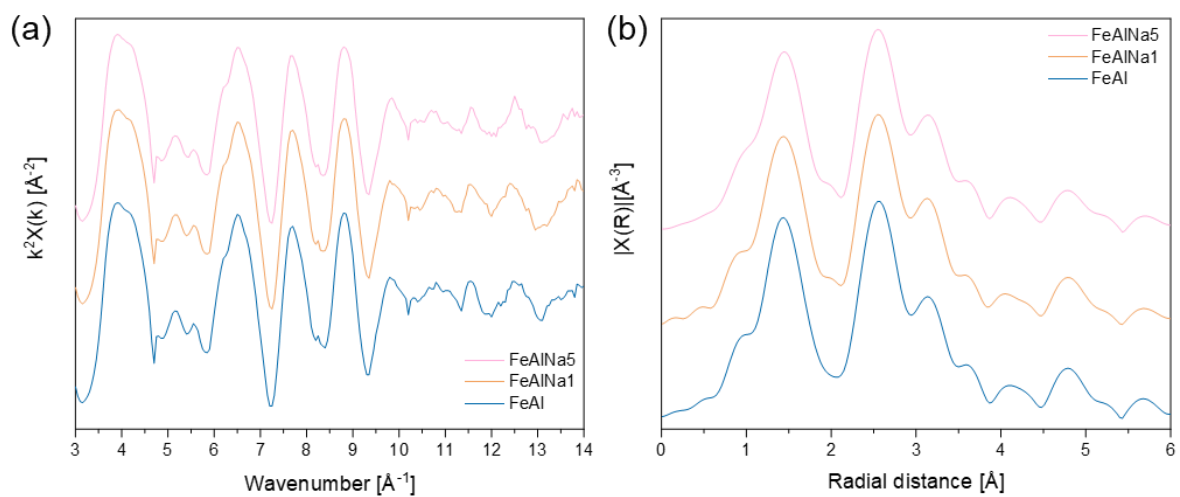


Figure S2: (a) k^2 -weighted EXAFS spectra and (b) Fourier transformed EXAFS functions (k^2 -weighted) of the calcined oxygen carriers measured at the Fe K-edge.

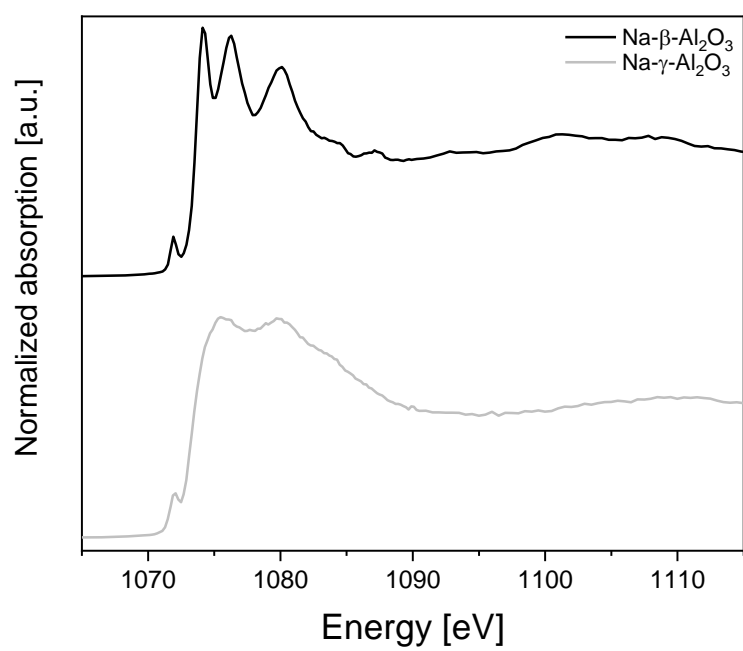


Figure S3. XANES spectra at the Na K-edge of the reference materials

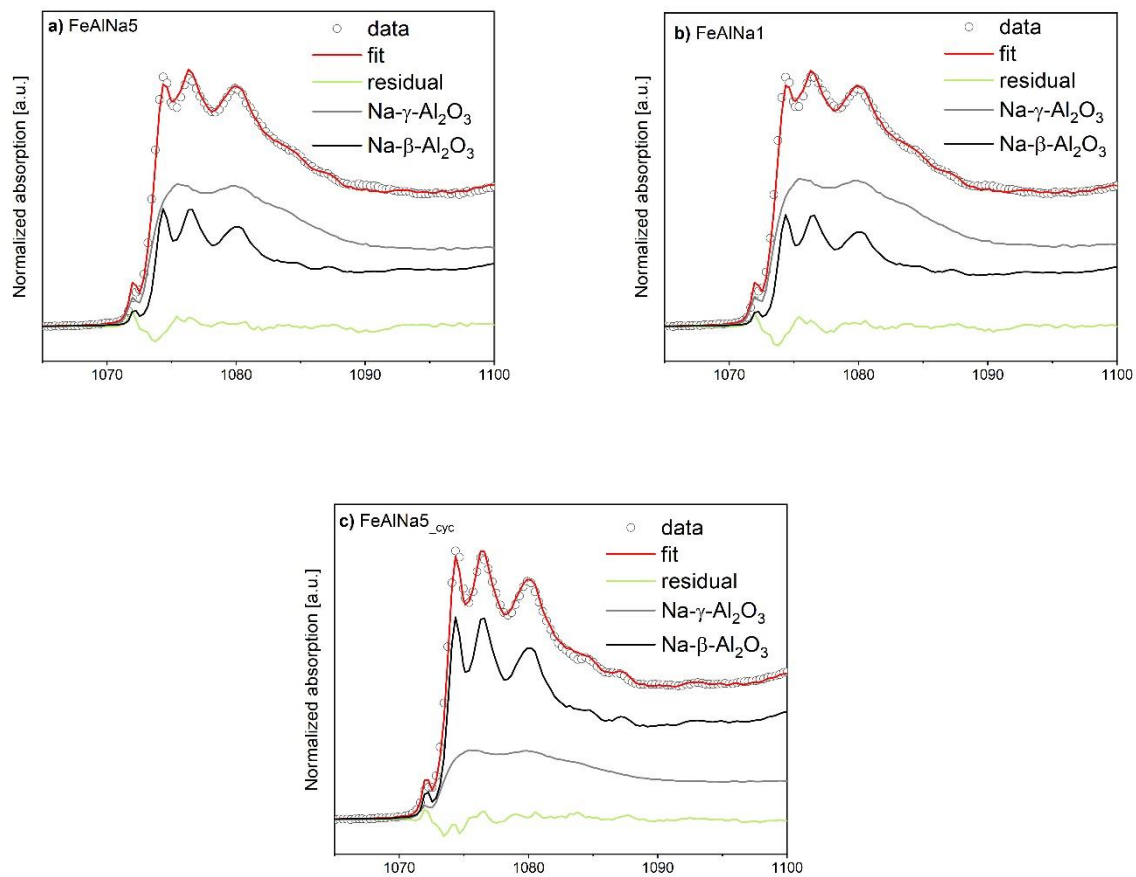


Figure S4. Linear combination fitting analysis of the Na K-edge spectra of FeAlNa5, FeAlNa1 and FeAlNa5_{cyc} using Na-β-Al₂O₃ and Na-γ-Al₂O₃ as references.

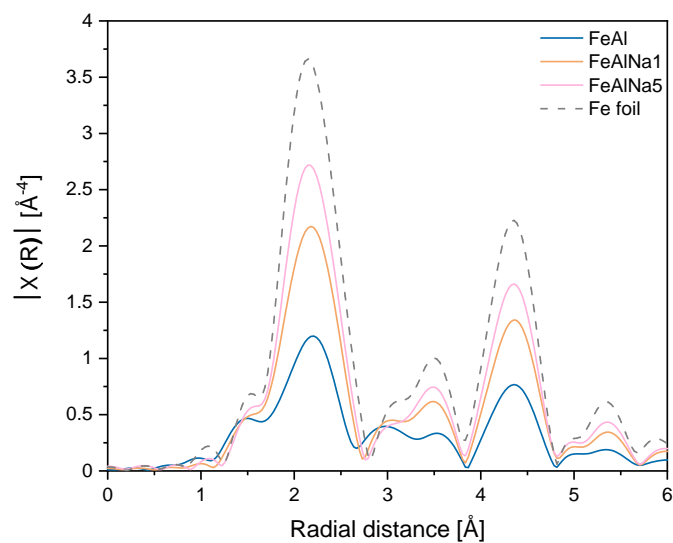


Figure S5. FT-EXAFS functions (k^3 -weighted) at the Fe K-edge of the cycled oxygen carriers.

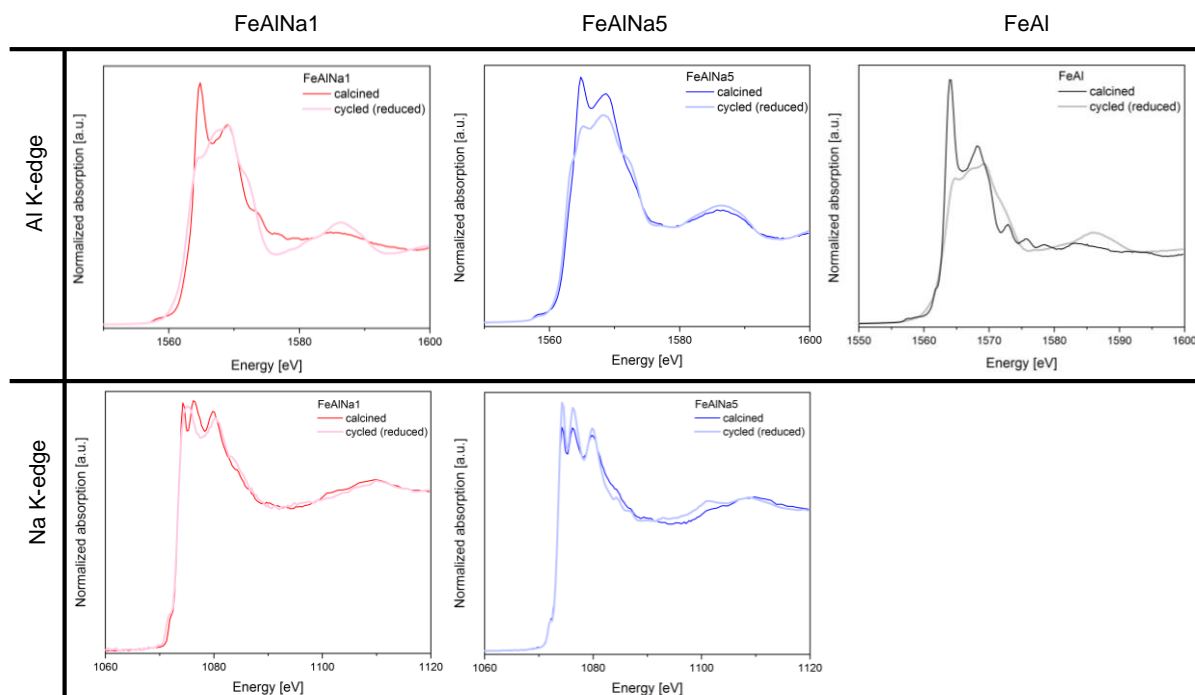


Figure S6. Comparison of the XANES spectra at the Na and Al K-edges of the materials before and after cyclic redox tests (15 cycles, reduced state).

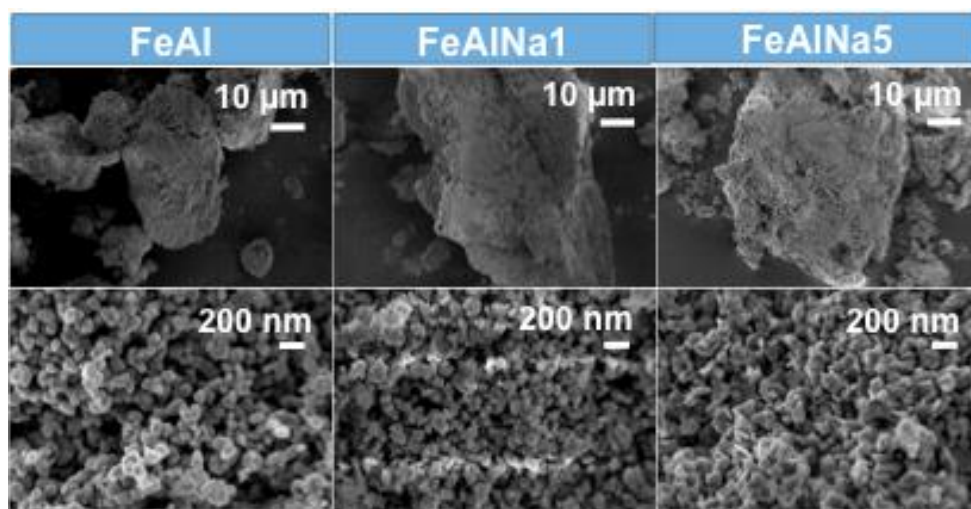


Figure S7: Electron micrographs of the calcined oxygen carriers.

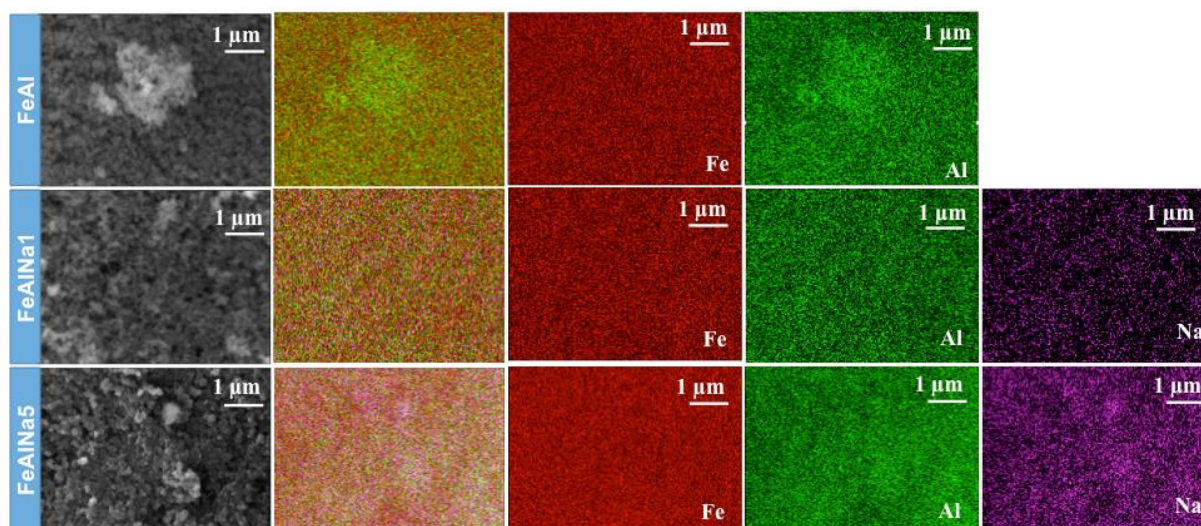


Figure S8: SEM/EDX maps of the calcined materials.

SEM images of the cycled materials after reduction (in 10 vol. % CO in N₂) and subsequent re-oxidation (in 23 vol. % H₂O in N₂ followed by 5 vol. % O₂ in N₂) are given in Figure S9. SEM images indicate that the oxygen carriers that showed a poor cyclic redox performance (FeAl and FeAlNa1) sintered after having been exposed to 15 redox cycles. The degree of sintering in FeAlNa5 was lower than that in FeAl and FeAlNa1 (over 15 redox cycles).

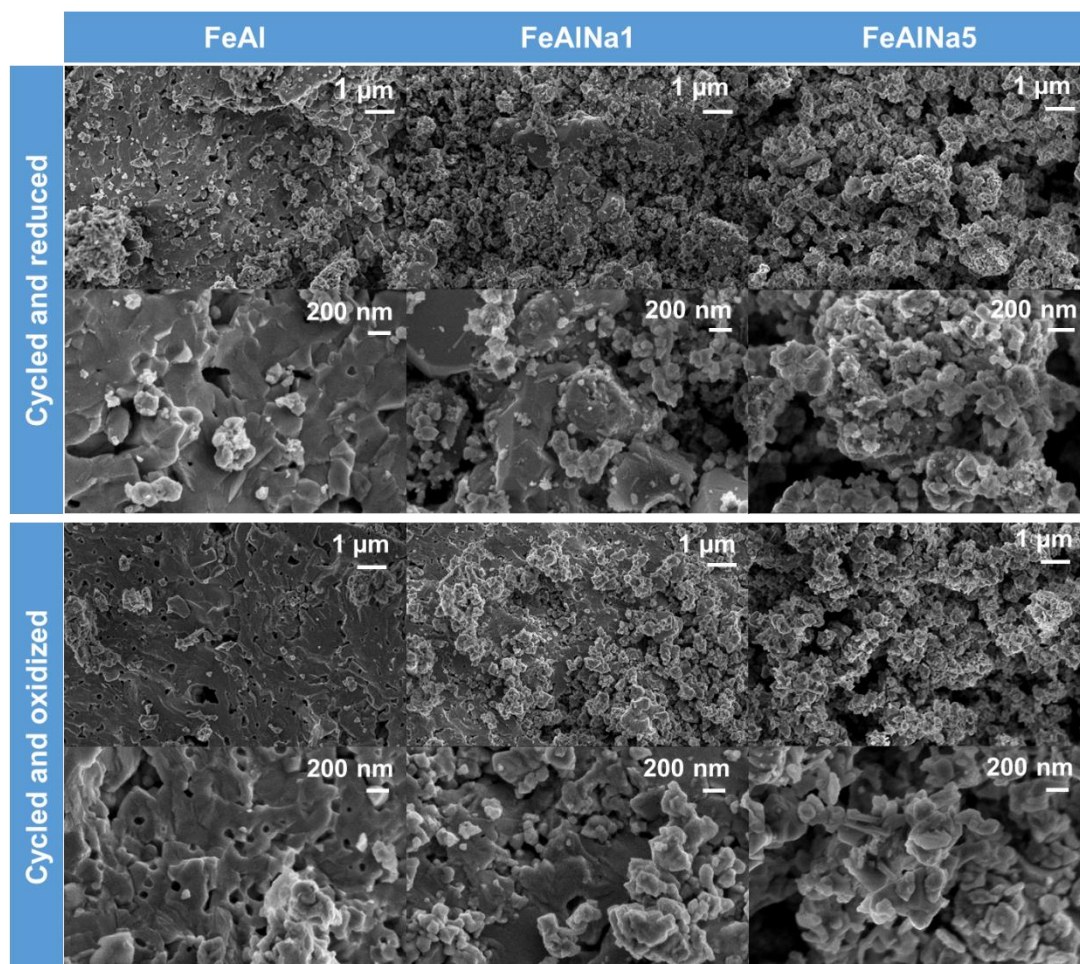


Figure S9: SEM of the cycled (reduced and oxidized states) oxygen carriers after being subjected to 15 redox cycles in a fixed bed.

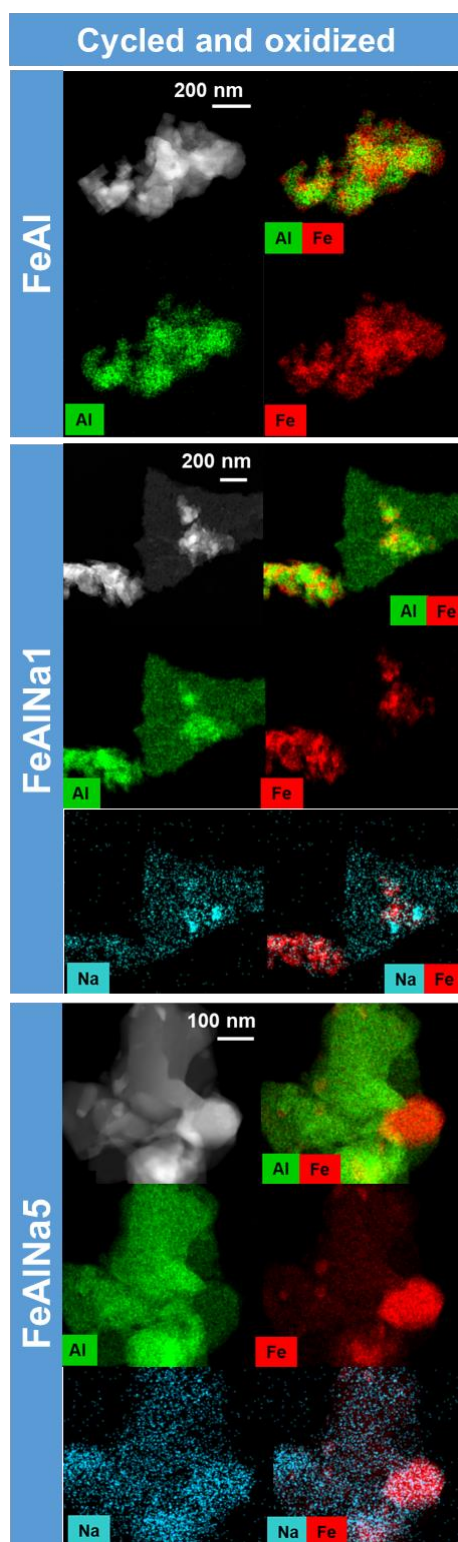


Figure S10: HAADF images and elemental mapping of the cycled oxygen carriers (15 redox cycles, oxidation step); $\text{H}_2\text{O}/\text{N}_2$ exposure followed by O_2/N_2).